Supplement of

Impact of in-cloud aqueous processes on the chemical compositions and morphology of individual atmospheric aerosols

Yuzhen Fu et al.

[*]*Correspondence to*: Guohua Zhang (zhanggh@gig.ac.cn) and Xinhui Bi (bixh@gig.ac.cn)

1 Air mass backward trajectories and meteorology conditions

The backward trajectory and the height (above sea level) of air masses during sampling were calculated by the Hybrid Single Particle Lagrangian Integrated Trajectory (HYSPLIT) model (http://ready.arl.noaa.gov). During three cloud events, the sampling site was greatly influenced by air masses from Southeast Asia, northern China and the South China Sea. Compared with the cloud event #1, the air masses of cloud event #2 and #3 passed through a relatively low path on the way to the sampling site. Thus, the air masses of cloud event #2 and #3 were affected more by the ground anthropogenic emissions. The ambient temperature at the sampling station varied from 12.1 to 18.6 °C during three cloud events, which means the generation of liquid cloud droplets. All samples were collected during the stable period of cloud events, when the mass concentration of $PM_{2.5}$ was less than 5 μg m^{-3} and visibility was less than 100 m. The concentrations of $PM_{2.5}$ during cloud event #1 were lower than those during cloud event #2 and #3. Consistently, the mean concentrations of O_3, SO_2 and NO_X were higher in the cloud event #2 and #3 (Table S3).

2 Identification of several components within RES and INT

Base on various element spectra, residual particles (RES) and interstitial particles (INT) were mainly classified as sulfate-rich (S-rich), carbonaceous material, mineral, metal, and fly ash (Twohy and Anderson, 2008;Li et al., 2016). Elemental compositions of S-rich were dominated by S, O, and some of them were associated with minor N, K and Na. Low intensity of N could be due to the evaporation of ammonia nitrate under the high energy electron beam (Smith et al., 2012). This led to the bubbly appearance of S-rich. It was found that the characteristic peaks of sulfate (*m/z* $-97HSO_4^-$) and nitrate (*m/z* $-46NO_2^-$ / $-62NO_3^-$) often coincide in the mass spectra of single RES and INT by SPAMS (Lin et al., 2017). In this case, S-rich represented secondary inorganic particles. The proportion of sulfate-containing particles was similar in the RES and INT (93% vs 94%). The elemental compositions of carbonaceous materials were characteristics of abundant C and minor O. Carbonaceous materials were divided into soot and OM according to different morphology. Soot were composed of tens to hundreds of carbon spheres ranging from 21 to 108 nm in diameter (average diameter was 47.7 nm), which often displayed botryoidal aggregates. OM did not have chain-like structure, which generally exhibited

amorphous state and spherical or irregular shapes. Mineral particles were consisted of Si, Al, Ca, O and minor Fe. Mineral were mainly clay, feldspar, calcite and gypsum, usually showing irregular shapes. Metal particles were represented as Fe, Zn, Ti, Mn, or Ni. Metal particles were characteristic of spherical, rectangular or irregular morphologies. They were largely from natural dust and industrial combustion (Silva et al., 2000;Ye et al., 2018). The presence of spherical metal particles indicated that they experienced melting at high temperature (Giere et al., 2003;Giere et al., 2006). Fly ash particles mainly contained Si, Al and O. Fly ash particles tended to be spherical in morphology and they were generally produced from the process of coal combustion (Chen et al., 2012; Henry and Knapp, 1980).

3 Influence of air masses on the distribution of particle types in the RES

The different air masses are expected to affect the distribution of particle types. The distribution of several types of particles in the RES were observed to be divergent in different cloud events, corresponding to different air masses, as shown in Figure S1 and Figure S2. The number fraction of OM-containing particles was the highest (81%) in cloud event #2, which might be partly attributed to the higher concentration of O_3 during cloud event #2 (Table S3). Higher solar radiation at the sampling time might also promote heterogeneous photochemical oxidation reactions during the cloud process and increased the generation of OM within cloud droplets (Xu et al., 2017). Aged metal particles accounted a similar percentage (7-12%) for three cloud events. The proportion of aged mineral during cloud event #1 (14%) was nearly four times those in the other two cloud events. Aged fly ash particles had the highest proportion (10%) in cloud event #3 compared with the other two cloud events, which is most probably influenced by the different air masses (Figure S2). Aged mineral particles of cloud event #1 may be influenced by the long-distance transportation of dust from Southeast Asia (Salam et al., 2003). Clearly, aged fly ash particles of cloud event #3 are associated with the air masses from the PRD region with a dense distribution of industrial facilities there (Cao et al., 2006).

4 The size distribution of RES and INT

In this study, a $PM_{2.5}$ cyclone inlet and a GCVI (ground-based counterflow virtual impactor) inlet were used to collect INT and RES, which is similar to (Cozic et al., 2007). Additionally, the particle size in this study is ECD (equivalent circle diameter) obtained from TEM images, which is larger than ESD

(equivalent spherical diameter). Liu et al. (2018) showed that the ECD of individual dry particles on the substrate is 0.4952 times that of the ESD.

The size distribution data shows a higher median diameter of RES (1.20 μm) than INT (0.63 μm) (Figure S6), which are higher than those (0.8 and 0.45 μm, respectively) at Mount Tai in northern China (Li et al., 2011). This could be due to that Mount Tai is located in an industrial area, whereas our site represents a background region mainly influenced by long-range transport. Additionally, the formation of secondary compounds during cloud events increase the size of RES (Zhang et al., 2017).

5 SPAMS analysis

A single particle aerosol mass spectrometry (SPAMS, Hexin Analytical Instrument Co., Ltd., Guangzhou, China) was used to analyzed chemical composition and size distribution of individual particles. Particles entering SPAMS were first focused into a beam of particles, and then their vacuum dynamic size were measured by two continuous diode Nd:YAG laser beams (532 nm). Next, the pulsed laser (266 nm) was precisely excited to ionize target particle according to the intrinsic velocity of each particle. Finally, we obtained the information of individual particles including vacuum dynamic particle size and the positive and negative ion mass spectrometry. The SPAMS is quite different from Aerodyne aerosol mass spectrometers (AMS). The latter can quantify the bulk chemical composition and size distribution of submicron nonrefractory aerosols (i.e. organic aerosol, sulfate, ammonium, nitrate and chloride), which obtain mass concentration of detected aerosols (Jimenez et al., 2003). Number fraction of several type particles can be known by SPAMS, which cannot gain mass concentration of several chemical compounds. However, for studying the chemical composition and mixing state of individual particles, the SPAMS is more useful.

All particles with bipolar mass spectra and the size range of d_{va} 0.1–1.9 μm were classified several clusters by an adaptive resonance theory neural network (ART-2a) with a learning rate of 0.05, a vigilance factor of 0.8 and 20 iterations, and merged similar clusters manually. Ten characteristic particle types (Figure S3) were obtained including BC (black carbon)-containing, OC (organic carbon), HMOC (highly molecular organic carbon), Dust, K-rich, Metal, Na-K, Amines, SS (sea salt) and Others. BC-containing particles are characterized by elemental carbon cluster ions (*m/z* $12C^{\pm}$, $24C_2^{\pm}$, $36C_3^{\pm}$, $48C_4^{\pm}$, …). OC particles mainly contain fragment ions of organics (*m/z* $27C_2H_3^+$, $37C_3H^+$, $43C_2H_3O^+$, -

26CN^-, …). The mass spectra of HMOC particles show the presence of peaks of OC particles and some other organic peaks (such as *m/z* 77$C_6H_5^+$, 91$C_7H_7^+$). Furthermore, HMOC particles are distinguished from OC particles by marked ion fragments detected in range of *m/z* > 100. Dust particles present significant ions at *m/z* 27Al^+, 40Ca^+ and 56CaO^+/Fe^+. K-rich particles are identified according to the strong signal at *m/z* 39K^+ only in positive mass spectra. Metal particles show the presence of metal ion peaks (such as Fe^+ (*m/z* 54 and 56), Mn^+ (*m/z* 55), Pb^+ (*m/z* 206, 207 and 208)) in positive mass spectra. Na-K particles are characterized by peaks at *m/z* 23Na^+, 39K^+, and less intense peaks at *m/z* -46NO_2^-, -62 NO_3^-, -97 HSO_4^-. The mass spectra of amines particles contain ions signals at *m/z* 59$N(CH_3)_3^+$, 86$C_5H_{12}N^+$, 101$C_6H_{15}N^+$. SS particles are mainly composed of ions peaks at *m/z* 23Na^+, 46Na_2^+, 62Na_2O^+, 63Na_2OH^+ and 81Na_2Cl^+. Most particles are observed to internally mixed with sulfate and nitrate (*m/z* -46, -62, -97). Particles with unconspicuous mass spectrum characteristics are named others. Specific classification criteria were described in detail elsewhere (Zhang et al., 2015).

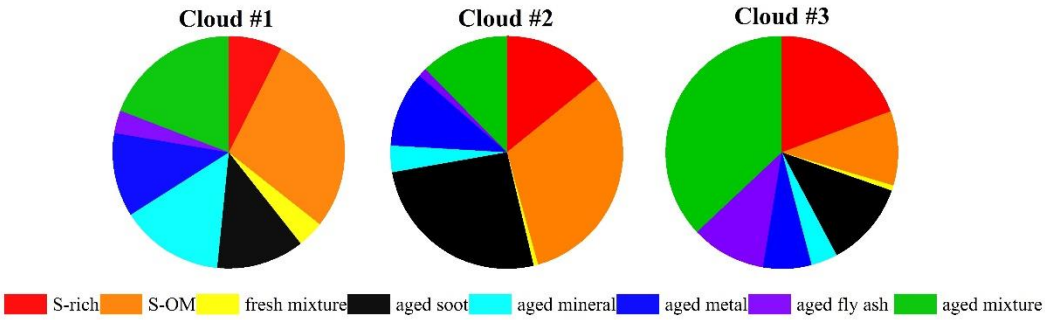

Figure S1. Number fraction of different particle types in the RES during three cloud events.

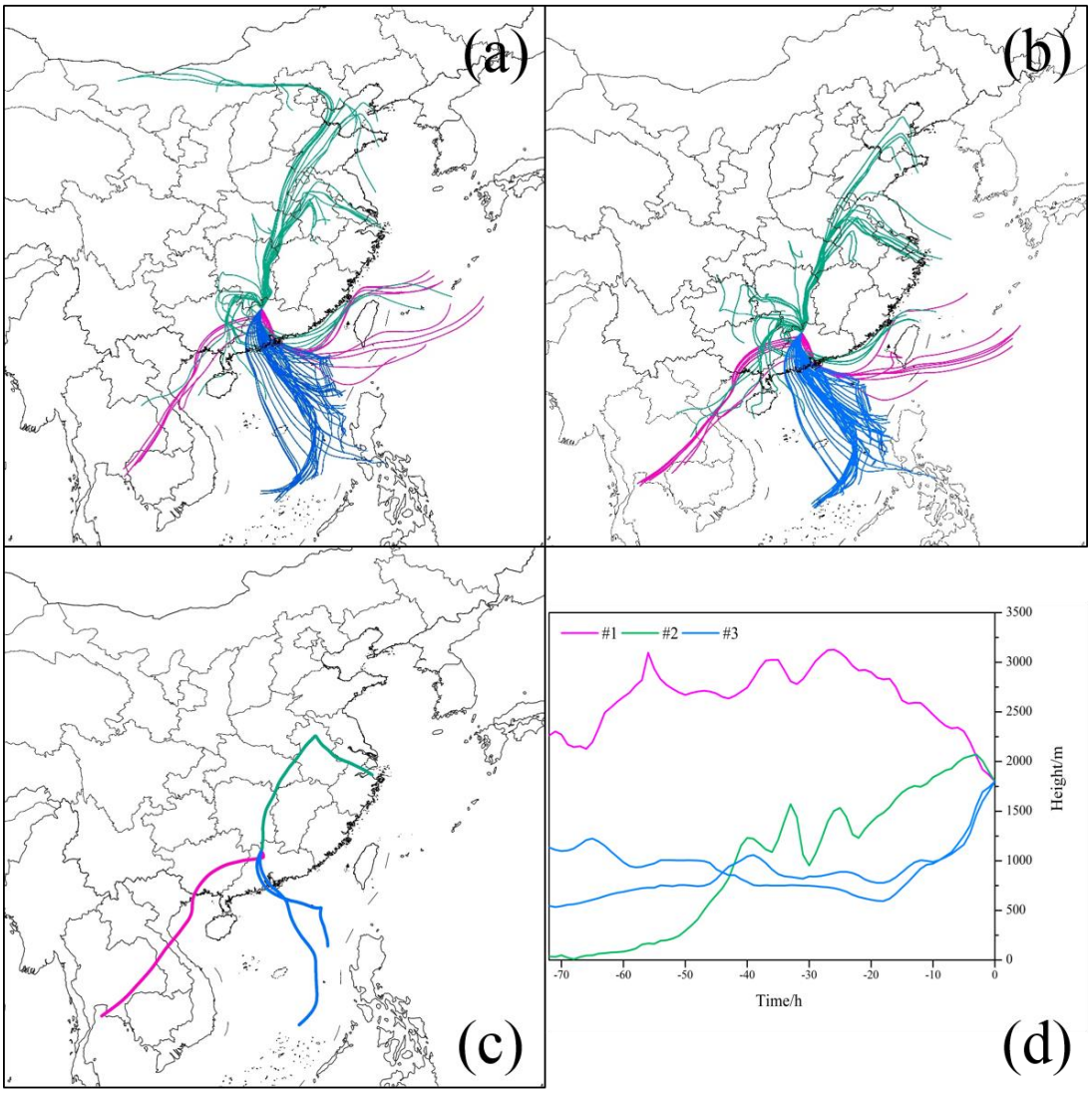

Figure S2. HYSPLIT back trajectories (72 h) for air masses arriving at our sampling site at the height of 1700 m (a) and 1800 m (b) hourly during the three cloud events. The HYSPLIT back trajectories at the height of 1800 m during sampling periods and heights (above sea level) of the air masses during transport (d). The horizontal axis represents several time points (0-72 h) before the time point input into the HYSPLIT model.

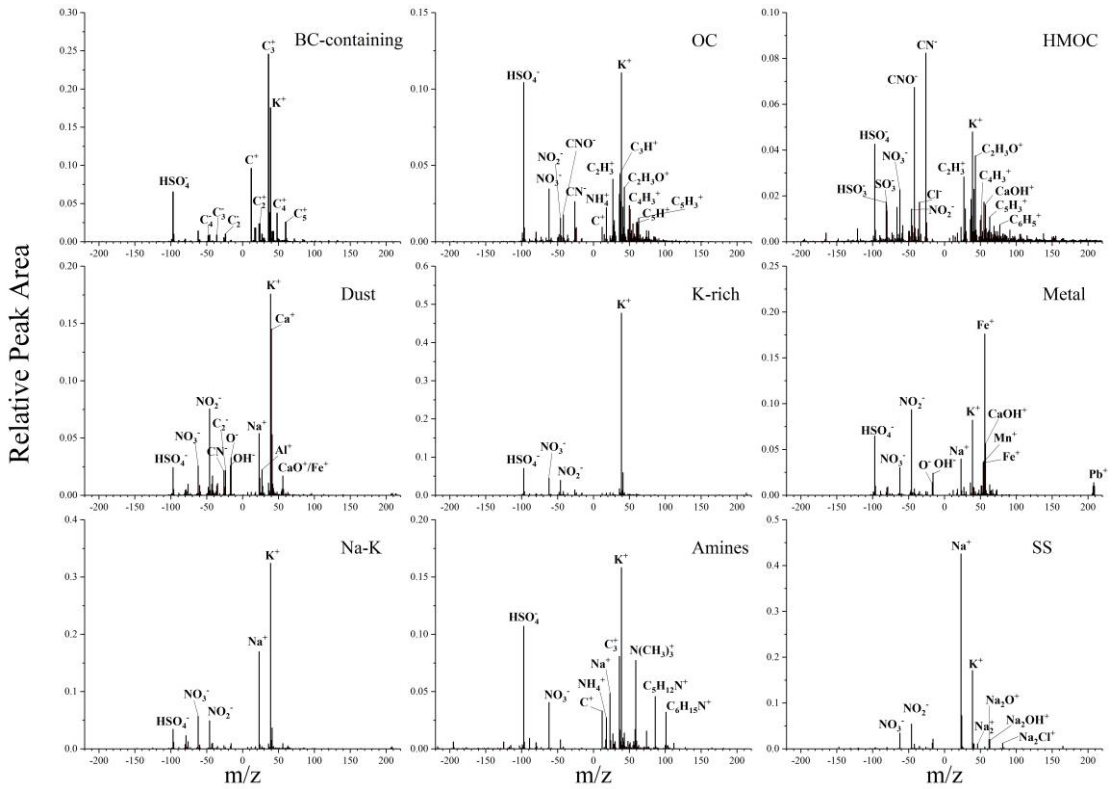

Figure S3. Average positive and negative mass spectra of main nine types particles (BC-containing, OC, HMOC, Dust, K-rich, Metal, Na-K, Amines, SS) measured by SPAMS.

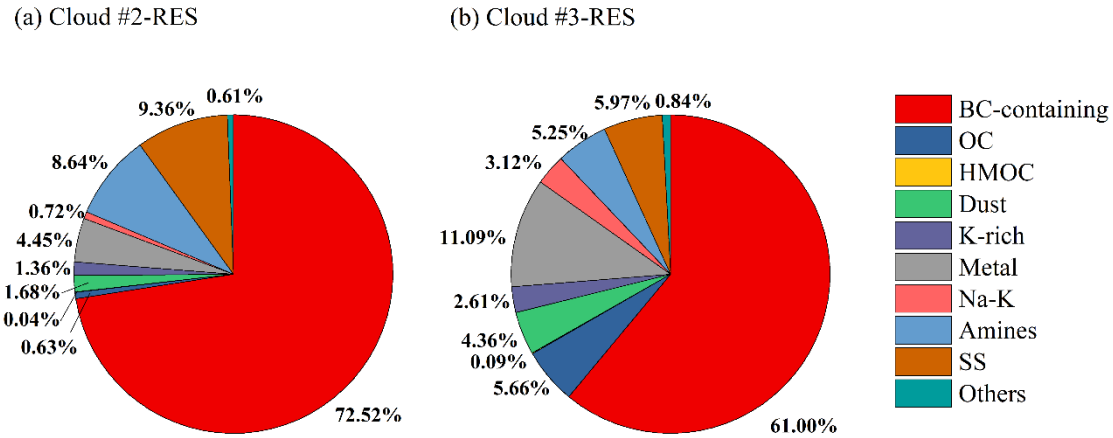

Figure S4. The chemical composition of RES during cloud event #2 and #3 measured by SPAMS.

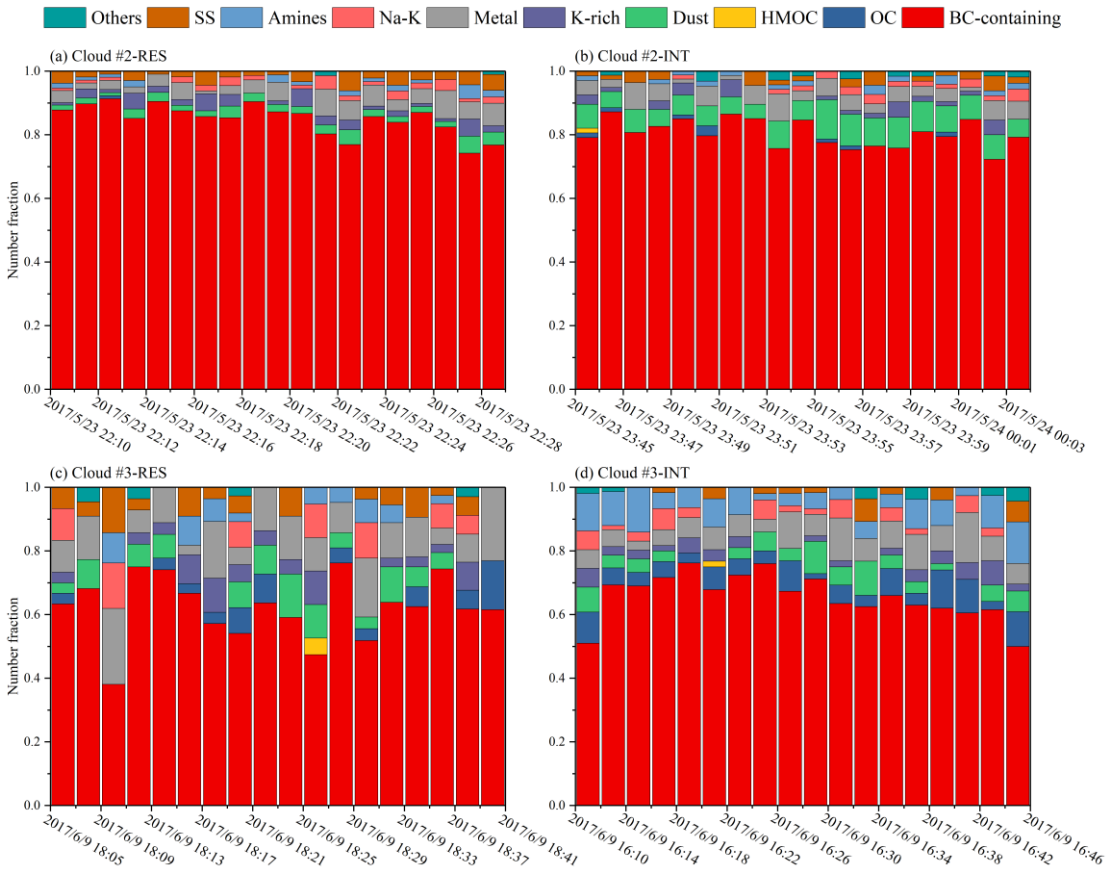

Figure S5. Time series of chemical composition of RES and INT during sampling periods of cloud event #2 and #3 measured by SPAMS.

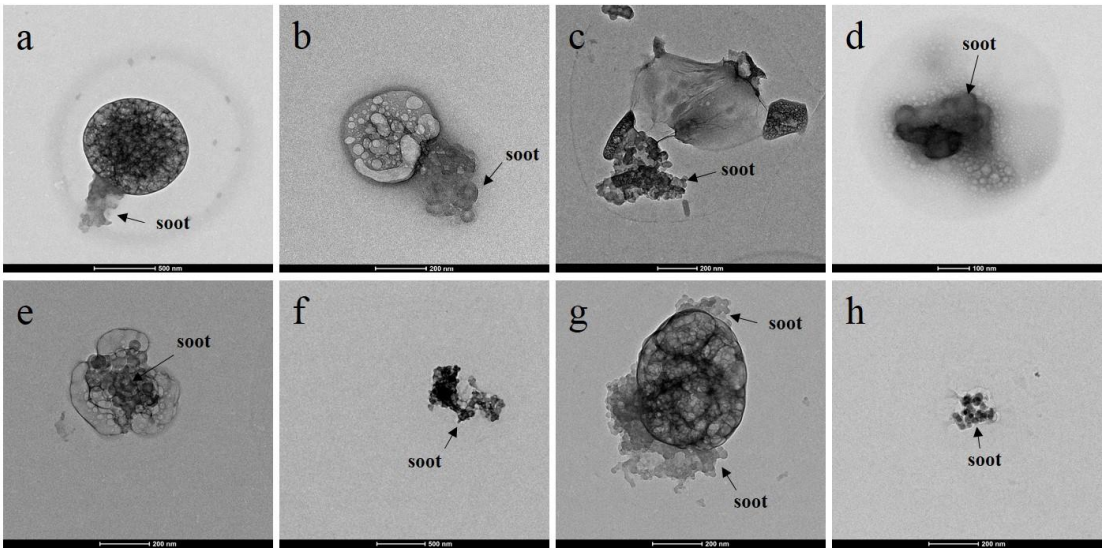

Figure S6. Typical TEM images of soot particles in the RES (a-d) and INT (e-h).

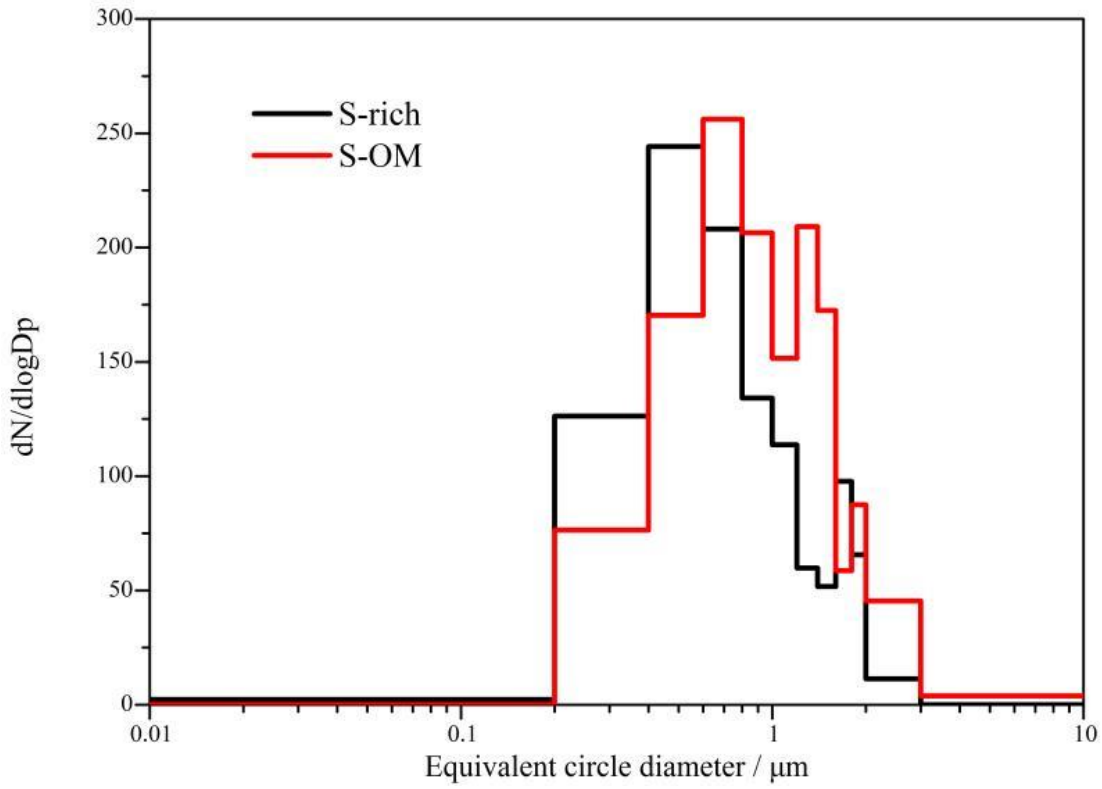

Figure S7. The size distribution of S-rich and S-OM particles. There are few S-rich particles with the size of less than 0.2 μm, and the median size are 0.56 μm and 0.76 μm for S-rich and S-OM particles, respectively.

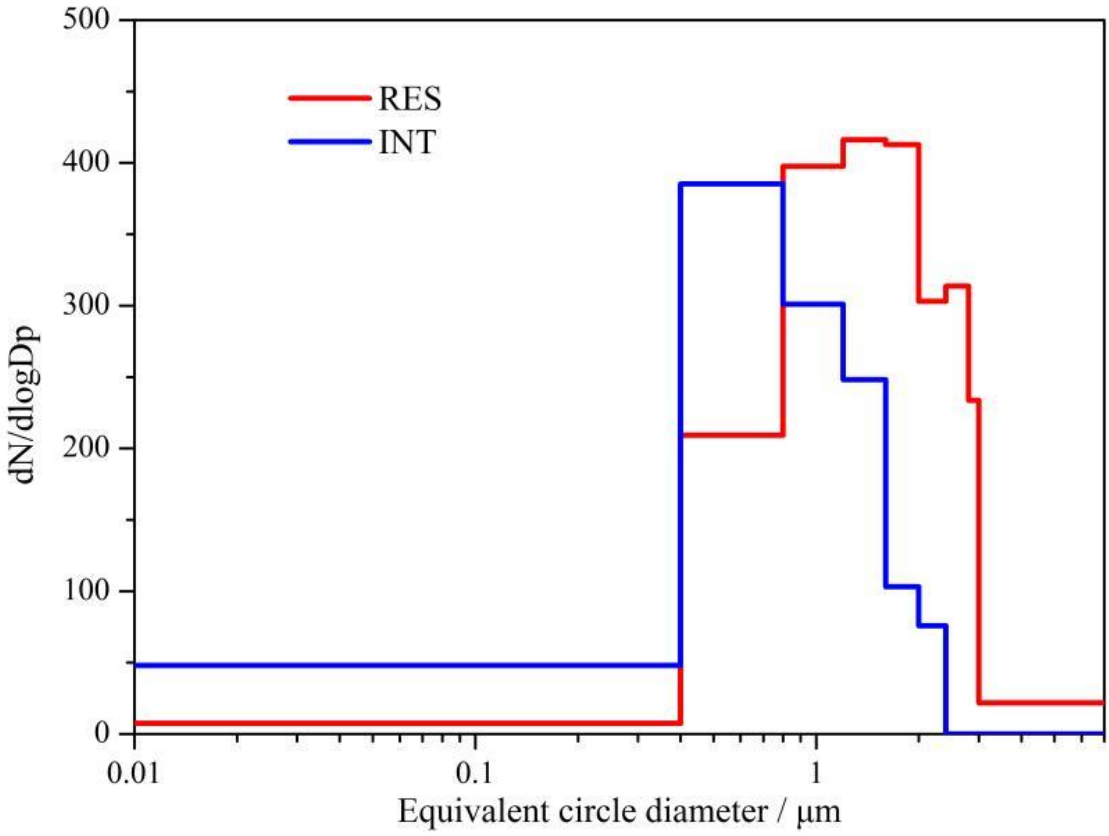

Figure S8. Size distribution of RES and INT during cloud event #2 and #3. There are more INT particles when the size is less than 0.8 μm, and more RES particles when the size is larger than 0.8 μm.

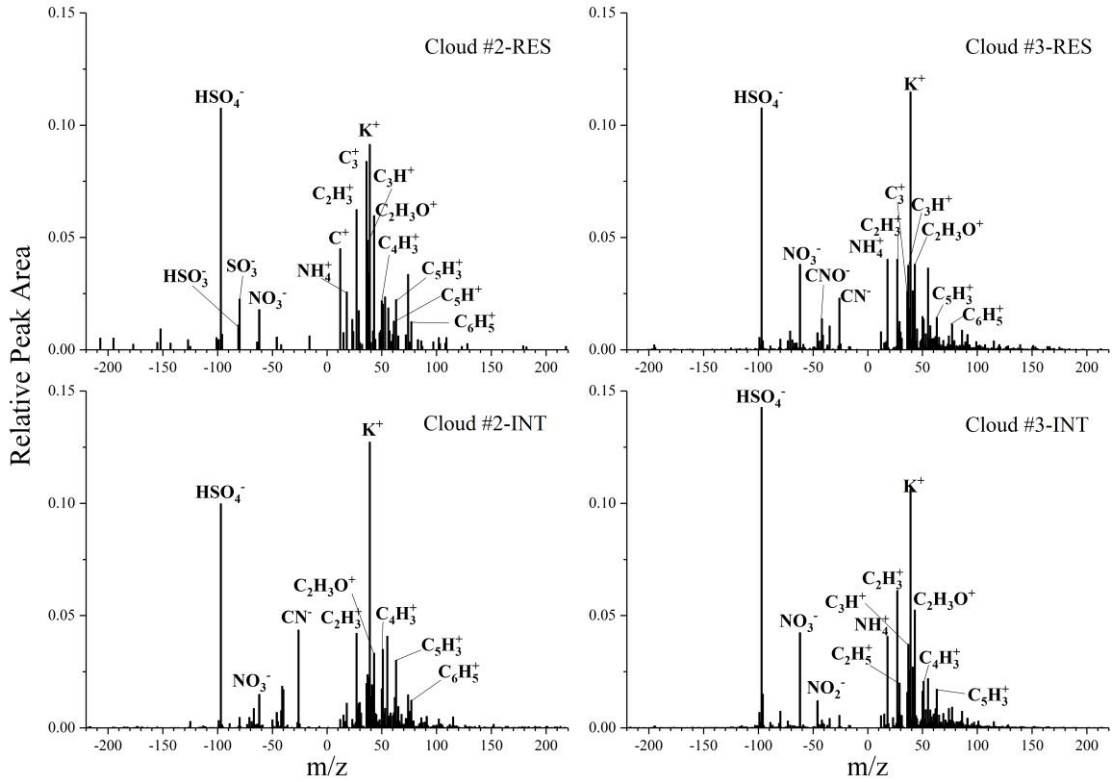

Figure S9. Average positive and negative mass spectra of OM particles (OC and HMOC) of RES and INT particles during cloud event #2 and #3 measured by SPAMS.

Table S1. The information of cloud events and samples, including starting and ending time of each cloud event, the number and type of analyzed particles, the mean value of visibility and number concentration of RES or INT during sampling time.

Cloud event	Starting Time*	Ending Time*	Particles	Type	Visibility/m	Number Concentration/cm^{-3}
Cloud #1	2017/5/20 18:19	2017/5/21 8:34	190	RES	66	195
Cloud #2	2017/5/23 20:35	2017/5/25 6:35	161	INT	50	99
			162	RES	88	299
Cloud #3	2017/6/8 18:30	2017/6/10 17:30	132	INT	44	996
			135	RES	33	111

* The time is the local time and that is Chinese Standard Time, UTC+8.

Table S2. The average value of O/C ratio of OM-containing particles with core-shell and coating mixing structures.

	coating	core-shell
RES	0.106	0.232
INT	0.076	0.056

Table S3. The concentration of NO_X, SO_2, O_3, PM_{10} and $PM_{2.5}$ during three cloud events.

cloud event	NO_X (ppb)	SO_2 (ppb)	O_3 (ppb)	PM_{10} (μg m^{-3})	$PM_{2.5}$ (μg m^{-3})
#1	2.6	0.4	30.5	3.6	1.1
#2	3.5	1.2	39.1	4.8	1.9
#3	4.3	0.6	34.4	11.4	4.7

Table S4. The ratios of relative peak area between organics (*m/z* 27, 29, 37, 43, 50, 51, 61, 63) and sulfate (*m/z* -97) of OM particles (OC and HMOC) during in-cloud (RES and INT) and pre-cloud (Ambient) periods.

	RES	INT	Ambient
Organics/Sulfates	1.676	1.566	1.594

Table S5. Morphological descriptors of soot particles within RES and INT.

parameters	A_p	d_p	L_{max}	N	D_f	k_g
RES	1658(175)	43(2)	255(12)	66(8)	1.82(0.12)	3.5(0.08)
INT	1842(133)	46(2)	316(16)	68(6)	2.11(0.09)	2.72(0.05)

A_p, mean projected area of the monomer; d_p, monomer diameter; L_{max}, maximum length of soot aggregates; N, number of monomers in a soot aggregate; D_f, mass fractal dimension; k_g, structural coefficient. In parentheses are the standard error of A_p, d_p, L_{max}, N, D_f and k_g.

Table S6. Overlap (δ), constant (k_a) and empirical exponent (α).

parameters	δ	k_a	α
RES	1.54	1.52	1.13
INT	1.4	1.44	1.11

References

Cao, G., Zhang, X., and Zheng, F.: Inventory of black carbon and organic carbon emissions from China, Atmospheric Environment, 40, 6516-6527, 10.1016/j.atmosenv.2006.05.070, 2006.

Chen, H., Laskin, A., Baltrusaitis, J., Gorski, C. A., Scherer, M. M., and Grassian, V. H.: Coal fly ash as a source of iron in atmospheric dust, Environmental Science & Technology, 46, 2112-2120, 10.1021/es204102f, 2012.

Cozic, J., Verheggen, B., Mertes, S., Connolly, P., Bower, K., Petzold, A., Baltensperger, U., and Weingartner, E.: Scavenging of black carbon in mixed phase clouds at the high alpine site Jungfraujoch, Atmospheric Chemistry and Physics, 7, 1797-1807, 10.5194/acp-7-1797-2007, 2007.

Giere, R., Carleton, L. E., and Lumpkin, G. R.: Micro- and nanochemistry of fly ash from a coal-fired power plant, American Mineralogist, 88, 1853-1865, 10.2138/am-2003-11-1228, 2003.

Giere, R., Blackford, M., and Smith, K.: TEM study of $PM_{2.5}$ emitted from coal and tire combustion in a thermal power station, Environmental Science & Technology, 40, 6235-6240, 10.1021/es060423m, 2006.

Henry, W. M., and Knapp, K. T.: Compound forms of fossil-fuel fly-ash emissions, Environmental Science & Technology, 14, 450-456, 10.1021/es60164a010, 1980.

Jimenez, J. L., Jayne, J. T., Shi, Q., Kolb, C. E., Worsnop, D. R., Yourshaw, I., Seinfeld, J. H., Flagan, R. C., Zhang, X. F., Smith, K. A., Morris, J. W., and Davidovits, P.: Ambient aerosol sampling using the Aerodyne Aerosol Mass Spectrometer, Journal of Geophysical Research-Atmospheres, 108, D7, 10.1029/2001jd001213, 2003.

Liu, L., Zhang, J., Xu, L., Yuan, Q., Huang, D., Chen, J., Shi, Z., Sun, Y., Fu, P., Wang, Z., Zhang, D., and Li, W.: Cloud scavenging of anthropogenic refractory particles at a mountain site in North China, Atmospheric Chemistry and Physics, 18, 14681-14693, 10.5194/acp-18-14681-2018, 2018.

Li, W., Li, P., Sun, G., Zhou, S., Yuan, Q., and Wang, W.: Cloud residues and interstitial aerosols from non-precipitating clouds over an industrial and urban area in northern China, Atmospheric Environment, 45, 2488-2495, 10.1016/j.atmosenv.2011.02.044, 2011.

Li, W., Sun, J., Xu, L., Shi, Z., Riemer, N., Sun, Y., Fu, P., Zhang, J., Lin, Y., Wang, X., Shao, L., Chen, J., Zhang, X., Wang, Z., and Wang, W.: A conceptual framework for mixing structures in individual aerosol particles, Journal of Geophysical Research-Atmospheres, 121, 13784-13798, 10.1002/2016jd025252, 2016.

Lin, Q., Zhang, G., Peng, L., Bi, X., Wang, X., Brechtel, F. J., Li, M., Chen, D., Peng, P., Sheng, G., and Zhou, Z.: In situ chemical composition measurement of individual cloud residue particles at a mountain site, southern China, Atmospheric Chemistry and Physics, 17, 8473-8488, 10.5194/acp-17-8473-2017, 2017.

Salam, A., Bauer, H., Kassin, K., Ullah, S. M., and Puxbaum, H.: Aerosol chemical characteristics of a mega-city in Southeast Asia (Dhaka-Bangladesh), Atmospheric Environment, 37, 2517-2528, 10.1016/s1352-2310(03)00135-3, 2003.

Silva, P. J., Carlin, R. A., and Prather, K. A.: Single particle analysis of suspended soil dust from Southern California, Atmospheric Environment, 34, 1811-1820, 10.1016/s1352-2310(99)00338-6, 2000.

Smith, S., Ward, M., Lin, R., Brydson, R., Dall'Osto, M., and Harrison, R. M.: Comparative study of single particle characterisation by Transmission Electron Microscopy and time-of-flight aerosol mass spectrometry in the London atmosphere, Atmospheric Environment, 62, 400-407, 10.1016/j.atmosenv.2012.08.028, 2012.

Twohy, C. H., and Anderson, J. R.: Droplet nuclei in non-precipitating clouds: composition and size matter, Environmental Research Letters, 3, 045002, 10.1088/1748-9326/3/4/045002, 2008.

Xu, W., Han, T., Du, W., Wang, Q., Chen, C., Zhao, J., Zhang, Y., Li, J., Fu, P., Wang, Z., Worsnop, D. R., and Sun, Y.: Effects of aqueous-phase and photochemical processing on secondary organic aerosol formation and evolution in Beijing, China, Environmental Science & Technology, 51, 762-770, 10.1021/acs.est.6b04498, 2017.

Ye, L., Huang, M., Zhong, B., Wang, X., Tu, Q., Sun, H., Wang, C., Wu, L., and Chang, M.: Wet and dry deposition fluxes of heavy metals in Pearl River Delta Region (China): Characteristics, ecological risk assessment, and source apportionment, Journal of Environmental Sciences-China, 70, 106-123, 10.1016/j.jes.2017.11.019, 2018.

Zhang, G., Han, B., Bi, X., Dai, S., Huang, W., Chen, D., Wang, X., Sheng, G., Fu, J., and Zhou, Z.: Characteristics of individual particles in the atmosphere of Guangzhou by single particle mass spectrometry, Atmospheric Research, 153, 286-295, 10.1016/j.atmosres.2014.08.016, 2015.

Zhang, G., Lin, Q., Peng, L., Bi, X., Chen, D., Li, M., Li, L., Brechtel, F. J., Chen, J., Yan, W., Wang, X., Peng, P., Sheng, G., and Zhou, Z.: The single-particle mixing state and cloud scavenging of black carbon: a case study at a high-altitude mountain site in southern China, Atmospheric Chemistry and Physics, 17, 14975-14985, 10.5194/acp-17-14975-2017, 2017.